Chemical Engineering Journal 423 (2021) 130203

Contents lists available at ScienceDirect

Chemical Engineering Journal

journal homepage: www.elsevier.com/locate/cej

Dynamically evolving 2D supramolecular polyaniline nanosheets for long-stability flexible supercapacitors

Yihan Wang [a,1], Xiang Chu [a,1], Zehao Zhu [a], Da Xiong [a], Haitao Zhang [a,*], Weiqing Yang [a,b,*]

[a] Key Laboratory of Advanced Technologies of Materials (Ministry of Education), School of Materials Science and Engineering, Southwest Jiaotong University, Chengdu 610031, PR China

[b] State Key Laboratory of Traction Power, Southwest Jiaotong University, Chengdu 610031, PR China

ARTICLE INFO

Keywords:
Polyaniline
Two-dimensional materials
Supramolecular crosslink
Flexible supercapacitors
Cycling stability

ABSTRACT

Highly pseudocapacitive conducting polyaniline (PANI) shows promising applications in flexible supercapacitors while suffer from low rate-capability and structural instability. The charging-discharging process with strong stress–strain behavior will unavoidably lead to the rapid break of PANI, badly restricting the cyclic stability of PANI-based supercapacitors. Herein, we employ a dynamically evolving emulsion polymerization strategy to elaborately construct two-dimensional (2D) secondary supraparticles polyaniline (ss-PANI) for greatly enhancing cycling stability of PANI-based supercapacitors. With dynamically evolving crosslink of aniline monomers and 1,4-phenylenediboronic acid, nanoparticles are firstly formed with the micelle action followed by demulsifying to transform into discrete platelets and further into 2D nanosheets via intermolecular hydrogen bonding. Ascribing to its excellent volume durability and the intermolecular hydrogen bonding effect, the greatly improved strain energy can efficiently restrict the volume change during repeatedly charging/discharging process. This 2D ss-PANI-based supercapacitors show a remarkable cycling stability of 93.9% capacitance retention over 10,000 cycles, which is far better than the previously reported PANI-based supercapacitors. Besides, the secondary supraparticles 2D structure endows PANI with rapid mass transfer rate that guarantees high specific capacitance (378 F g^{-1}) and high rate-capability. Undoubtedly, this research can guide the design of electrochemically dynamics-enhanced conducting polymers for the high-stability flexible supercapacitors as well as the portable energy storage devices.

1. Introduction

Flexible devices such as flexible display, portable electronic devices, wearable devices, electronic sensors and personal medical monitors have emerged in our daily life and are rapidly pushing modern society into the era of Internet of Things [1–3]. However, the development of flexible energy storage devices is still far behind the energy demand of billions of flexible electronics [4–5]. In this regard, flexible supercapacitors (FSCs) have recently received wide attentions due to the advantages of excellently mechanical flexibility, high safety, and fast charging-discharging rate [6–10].

In general, high capacitance electrode material is the key factor for high-performance supercapacitors [11]. Polyaniline (PANI), as a typical kind of high-performance pseudocapacitance electrode material, is a structural diversification conductive polymer electrode combining the synergistic advantages of traditional polymer materials and organic conductors [12–14], and naturally possesses a high theoretical specific capacitance of ~ 2,000 F g^{-1} [15]. While for nano-structured PANI, the greatly-improved specific surface area and substantially-added surface-active sites will remarkably enhance their capacitive and rate-capability properties [16–18]. Nevertheless, the volume expansion effect during long-term charging/discharging processes will unavoidably lead to poor electrochemical stability, badly hindering its practical application in supercapacitors [19,20]. Hence, it is of great urgency to improve the cyclic stability of nano PANI electrode materials and supercapacitors [21].

So far, the stability of polyaniline-based supercapacitors could be improved by means of nano-compounding strategy. Jiang et al., [22]

* Corresponding authors at: Key Laboratory of Advanced Technologies of Materials (Ministry of Education), School of Materials Science and Engineering, Southwest Jiaotong University, Chengdu 610031, PR China.
E-mail addresses: haitaozhang@swjtu.edu.cn (H. Zhang), wqyang@swjtu.edu.cn (W. Yang).
[1] These authors contributed equally to this work.

https://doi.org/10.1016/j.cej.2021.130203
Received 5 December 2020; Received in revised form 2 April 2021; Accepted 30 April 2021
Available online 7 May 2021
1385-8947/

utilized the in-situ assembly of PANl conductive layer on the surface of the well-crystallized α-MoO_3 to obtain the composite PANl/MoO_3 nanobelts, capacity retention of which was 76.7% after 3,000 charge/discharge cycles. Although this nanostructured composite electrode improved the structural changes of PANI to a certain extent [23], its cyclic stability is difficult to meet the widely commercial requirement of long-lived PANI-based supercapacitors. The corresponding reasons are as follows: (i) mechanical expansion upon ion insertion; (ii) delamination of electrode materials from substrates; (iii) the fibrous morphology of the polyaniline. This fibrously structured polyaniline easily results in structural failure during the redox reactions with harsh and frequent phase variations. Except those, the poor dispersion ability of PANI in the composite material and the excessively complex preparation process of adding the secondary or even third phases are also common issues for the practical application of PANI.

In this work, we report a dynamically evolving emulsion polymerization strategy to elaborately construct two-dimensional (2D) secondary supraparticles polyaniline (ss-PANI) (Figure S1) by employing 1, 4-phenylenediboronic acid (1, 4-PDBA) to fundamentally solve its traditional volume expansion and counterion drain effect. Due to its excellent volume durability and the intermolecular hydrogen bonding effect, the substantially enhanced strain energy can efficiently suppress the volume expansion effect during repeatedly charging/discharging process, so as to solve the problem of intrinsically electrochemical instability of conducting polymers. Cycling stability of ss-PANI based flexible supercapacitors is demonstrated by 93.9% capacitance retention over 10,000 galvanostatic charging/discharging cycles. Besides, the unique structure facilitates rapid mass transfer and hence ss-PANI deliver a high specific capacitance of 378 F g^{-1} and a high rate-capability. Therefore, this work provides a novel strategy for designing high-stability conducting polymer-based flexible supercapacitors, which will underpin next-generation flexible power supplies.

2. Results and discussion

Fig. 1**a** schematically illustrates the structure of 2D ss-PANI. Indeed, TEM (Fig. 1b) and SEM (Fig. 1c) images of 2D ss-PANI nanosheets obviously present their abundant secondary structures with lots of nanoscale convex targets on the surface of nanosheets. Such unique structure should be mainly ascribed to the intermolecular hydrogen bonds action between 1, 4-PDBA and PANI. During emulsion polymerization process, 1, 4-PDBA is utilized as both crosslinker and dopant. On one hand, the hydroxyl of boronic acid groups from 1, 4-PDBA can crosslink with the amino groups from the PANI molecular chain for the formation of hydrogen bonds. Pure PANI without adding 1, 4-PBDA could not form a gelation as shown in Figure S2, indicating that the 1, 4-PBDA acts as a crosslinker to promote the gelation by supplying additional hydrogen bonds. On the other hand, the boronic acid groups from 1, 4-PDBA can be additionally used as the dopant to be doped into PANI chains. Thus, both electrostatic interaction and hydrogen bonds would interconnect 1, 4-PDBA molecules and PANI chains. Such strong interactions can play important roles in crosslinking 1D PANI molecular chains into 2D nanosheets through supramolecular action (Fig. 1d). Moreover, as shown in Figure S3 and Figure S4, the morphology between pure PANI and ss-PANI shows a huge difference. The pure PANI without adding 1, 4-PBDA appears coral-like structures, while with the help of 1, 4-PBDA, the typical fiber-like PANI further crosslinks into 2D sheets, which again verifies that 1, 4-PDBA plays a crucial role in the process of self-assembly.

To unravel the exact formation mechanism, we discussed growth processes with different reaction time and concluded that the growth dynamics based on forward microemulsion polymerization and supramolecular co-effects lead to the unique 2D ss-PANI. Due to the amphiphilicity of 1, 4-PDBA (Figure S5), the hydrophilic boric acid group makes molecule have the tendency to enter water, while the hydrophobic benzene ring chain tries its best to prevent it from dissolving in water and tends to escape from the water phase. With the addition of aniline monomer, 1, 4-PDBA quickly adsorbed on aniline. The surface of aniline is adsorbed and covered by 1, 4-PDBA with the increase of assembly time, aggregating spherical micelles with 1, 4-PDBA outside and aniline inside in the solution (Fig. 2**a-b**). Dynamic equilibrium of hydrophilic and hydrophobic effect of 1, 4-PDBA leads gradual decrease in surface tension. Once the interaction force between 1, 4-PDBA and PANI gained upper hand, the above-mentioned surface tension would be efficiently inhibited. This effect resulted in the damage of micro-reactors formed by water/oil interface, leading to micellar demulsification [24] (Fig. 2c). Due to the depleting of aniline monomers and oxidant, in the center of the nucleation formed a completely around the consumption area, and free aniline monomers and antioxidants cannot be timely supplemented. Thus, polyaniline can only grow in the part of the

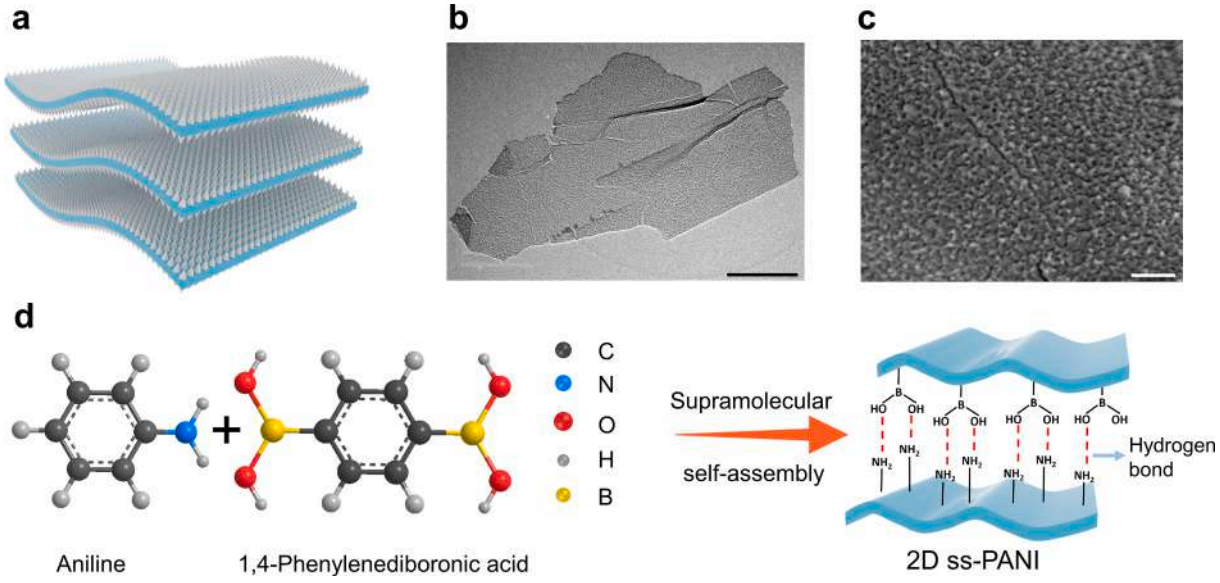

Fig. 1. A supramolecular assembling strategy to construct ss-PANI nanosheets. (a) Schematically illustrating the structure of 2D ss-PANI. (b) TEM and (c) SEM images of 2D ss-PANI nanosheets, indicating their abundant surface secondary structures. (d) Supramolecular crosslinking aniline with 1, 4-PDBA to synthesize 2D ss-PANI consisting of numerous hydrogen bonds. The scale bars in Fig. 1b and 1c are 2 μm and 200 nm, respectively.

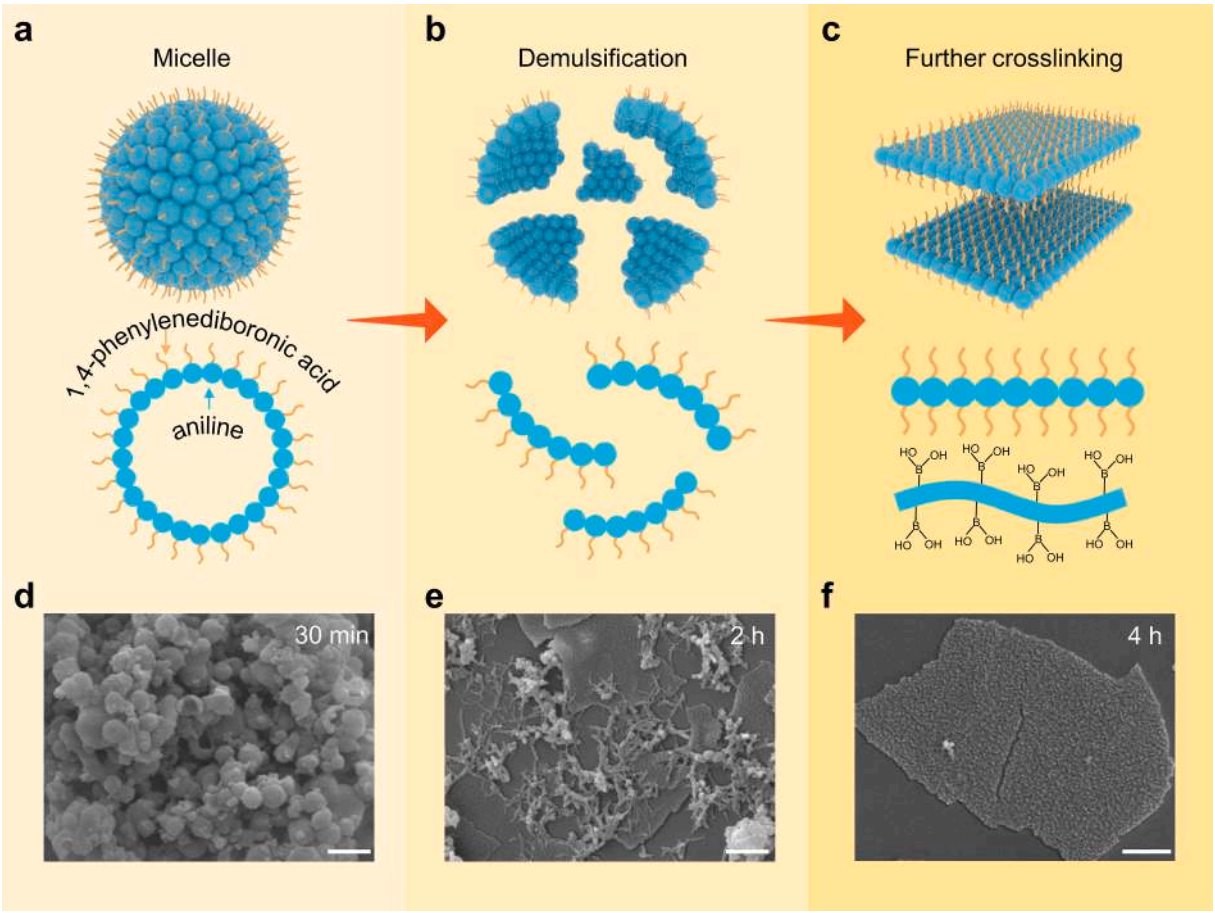

Fig. 2. The growth mechanism of ss-PANI nanosheets. (a) Micelle, (b) Demulsification, (c) Further crosslinking. SEM images of samples with different reaction time of (d) 30 min, (e) 2 h and (f) 4 h. Scale bars, 500 nm in b, d, f.

consumption area along the direction of one dimensional (anisotropic growth) and gradually grow into nanometer fiber, which can be clearly observed from the SEM image (Fig. 2d). The fiber-like morphology of PANI (marked by red ellipse) should be present at the yielded PANI flakes at the early stage of 2 h (Figure S6a, c, e, f). In Figure S6b, these fiber-like PANI had already begun to partially self-assemble into 2D film-like PANI. It should be noted that the diameter size is much smaller than that of nanospheres, implying that a new polymerization should begin with the breaking of the previously formed nanospheres instead of directly forming fibers [25].

With the help of supramolecular interaction supplied by 1, 4-PDBA and PANI, the further crosslinking would be occurred with the prolonging reaction time (upper section of Fig. 2e). As anticipated, hydrogen bonding and π-π electron interactions provide the driving force for self-assembly, which in turn assemblies the remaining fibers into flake structures (bottom of Fig. 2e) [26], and finally into 2D nanosheets (Fig. 2f). Its surface is easy to become the nucleation center of subsequent polymerization of PANI, which causes secondary growth, resulting secondary structure with rough surface [27–32]. SEM of the conversion process of nanospheres to fiber and plate-like ss-PANI can be seen in Figure S7.

As indicated in TG tests (Figure S8), the first weightlessness stage of ss-PANI starts from 0 to 100 °C, only lost a small part of the mass, with a weightlessness mass fraction of 22%. The reason could be the evaporation of water molecules physically adsorbed on the surface and the volatilization of other low-molecular weight substances. In the second stage, the weight loss was 27.5% with the temperature up to 700 °C, which is mainly due to the degradation of PANI. This slow weight loss rate in whole process evidently reveals that the hydrogen bonds between PANI molecular chains can effectively enhance the thermal stability of ss-PANI. Therefore, incorporation of 1, 4-PDBA facilitates the formation and also promotes the thermal endurance of 2D ss-PANI [33,34].

After supramolecular crosslinking, the ss-PANI gel exhibits the characteristic of PANI conducting polymers. The electrical conductivity of ss-PANI is about 1 S m^{-1}. Meanwhile, the ss-PANI replicated the crystalline of PANI while the (0 2 0) diffraction peak becomes stronger for ss-PANI than pure PANI (Figure S9). The increased intensity of (0 2 0) in ss-PANI may be related to the further orientation of 2D platelets in comparison with fiber-like structure [35]. All in all, the growth dynamics based on emulsion method and supramolecular crosslink substantially facilitates structural evolution and eventually leads to 2D ss-PANI.

After introducing the 1, 4-PDBA, the hydrophilicity of ss-PANI is greatly improved. This is mainly due to a majority of the formed hydrogen bonds from the partial ionization of H^+ in boric acid groups. Besides, ss-PANI presents the excellent dispersibility, which can be obviously verified by its Tyndall effect of colloidal aqueous solution with a concentration of 0.25 mg mL^{-1}. In contrast, pure PANI will precipitate in the bottom of the vial rapidly (Fig. 3**a** and Movie S1).

As shown in Fig. 3b, the ss-PANI nanosheets demonstrate the stacked structure. Obviously, the ss-PANI nanosheets share promising uniformity and large lateral size of several micrometers to a dozen micrometers. Notably, some wrinkles can be detected on the surface of 2D ss-PANI nanosheets, indicating high flexibility of the nanosheets (Figure S10). Fig. 3c shows overt mastoid protrusion on the rough surface of the nanosheets attributed to secondary growth of PANI, which can be further verified by the transmission electron microscopy (TEM) (Fig. 3d). As a result, the protrusion array revealed by TEM image is in

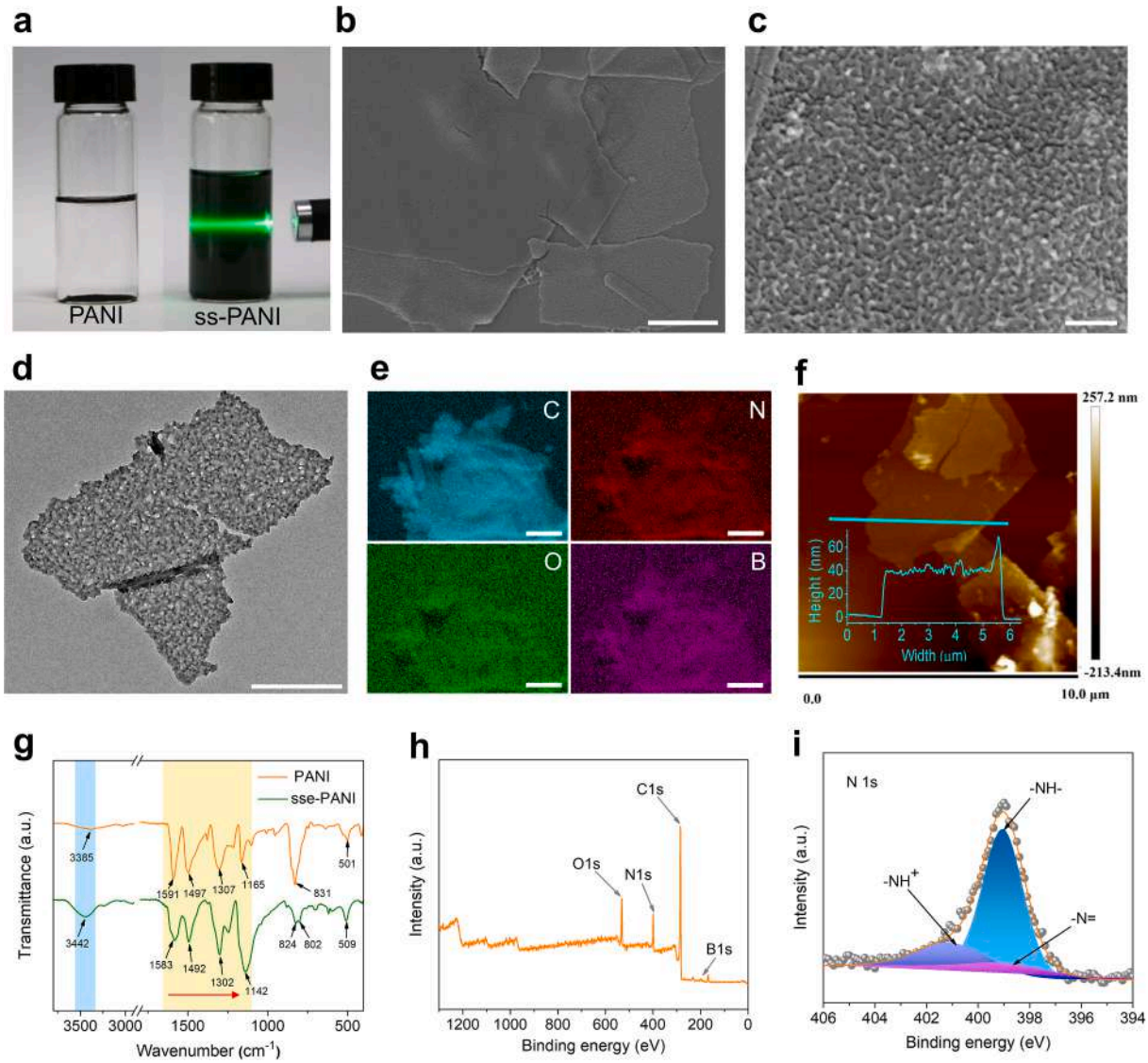

Fig. 3. Morphology and chemical compositions of ss-PANI. (a) Pure PANI and ss-PANI aqueous solutions were stood for 3 weeks. (b) Low- and (c) high-magnification SEM micrographs of ss-PANI. (d) TEM images of ss-PANI. (e) EDS mapping of ss-PANI. (f) AFM image of ss-PANI and inset is height profile of the nanosheet. (g) FTIR spectra of pure PANI and ss-PANI. (h) XPS wide scan spectra of ss-PANI. (i) N1s deconvoluted spectra of ss-PANI. Scale bars, 2 μm in b, 0.2 μm in c, 0.5 μm in d, and 10 μm in e.

good agreement with that of SEM images. On one hand, the mastoid protrusion array can remarkably increase the ion-accessible surface area, on the other hand, more active sites of electrochemical redox reaction can be provided, thus leading to a more efficient electrochemical process [36]. EDS analysis shows the relatively uniform distribution of C, N, O, B elements in ss-PANI (Fig. 3e). According to the atomic force microscopy (AFM) characterization, the thickness of ss-PANI nanosheet is around 50 ± 15 nm (Fig. 3f), indicating the thickness of 2D ss-PANI is not very susceptible to the concentration of 1, 4-PDBA and has good consistency (Figure S11).

The molar ratios of 1,4-PDBA to aniline is 1:1, 1:2, 1:3, 1:4, 1:5, 1:6, 1:8, 1:10, 1:15, 1:20. The key factor affecting morphology is aniline concentration (Figure S12-S14). The morphology is spherical at 1:1,1:2,1:3; flake-like at 1:4,1:5,1:6; interwoven irregular sheet at 1:8, blocky structure at 1:10 and 1:20. The thickness of sheets were about 50 ± 5 nm at 1:4, 20 ± 5 nm at 1:5 and only about 8 nm at 1:6. Evidently, the higher aniline concentration, the thinner lamellar.

In order to analyze the chemical compositions of ss-PANI nanosheets, we have tested the FTIR spectrum of both pure PANI and ss-PANI nanosheets. Generally, ss-PANI duplicates the infrared characteristic of PANI, as indicated by the adsorption of N–H bonds (3,385 cm^{-1}), the C=C stretching vibration of quinoid ring (1,591 cm^{-1}) and benzenoid ring (1,497 cm^{-1}), aromatic C-N stretching vibration (1,307 cm^{-1}), as well as aromatic C–H in-plane (1,165 cm^{-1}) and out-plane (831 cm^{-1}) bending vibration (Fig. 3g). However, there are two distinct changes between pure PANI and ss-PANI. One is the occurrence of an apparent red-shift as highlighted by a yellow background for 2D ss-PANI in comparison with pure PANI, which is ascribe to the hydrogen bond interaction between 1, 4-PDBA and PANI chains. Another is that 2D ss-PANI exhibits a much more intensive peak at around 3442 cm^{-1}, which can be attributed to the overlap of O–H bond in 1, 4- PDBA and N–H bond in PANI as marked by a blue shaded region.

The surface chemical compositions of 2D ss-PANI were further determined by X-ray photoelectron spectroscopy (XPS). Presence of oxygen (O1s, ~528 eV), nitrogen (N1s, ~401 eV), carbon (C1s, ~285 eV) and boron (B1s, ~189 eV) can be confirmed (Fig. 3h). Element carbon is derived from the PANI backbone and 1,4-PDBA. Elements oxygen and boron mainly come from 1,4-PDBA. What is noteworthy is that an amount of B1s peak can be detected, indicating efficient cross-link of 1,4-PDBA with PANI. And the N1s core level peak originated from

PANI can also be detected. The peaks with binding energies (BEs) of 398.35 eV, 399.01 eV, 401.11 eV correspond to quinone di-imine nitrogen (=N-), di-amine nitrogen (–NH-) and proton doped nitrogen ($–NH^+$) through deconvolution of N1s spectrum (Fig. 3i). A high level of proton doped nitrogen ($–NH^+$) (~20%) (Table S1, Supporting Information) implies that the PANI polymeric chains are successfully doped by 1, 4-PDBA, again emphasizing the existence of statistic supramolecular interaction between PANI and 1, 4-PDBA.

Since the surface of ss-PANI nanosheets contains abundant hydrophilic boronic acid groups on the surface, the ss-PANI shows greatly improved hydrophilicity. A low contact angle of 24° appears in ss-PANI while pure PANI show a large contact angle of 72° (Fig. 4**a**). The specific method of sample preparation for a water contact angle test can be seen in Figure S16. Therefore, the ss-PANI nanosheets can be well dispersed in water to form stable ss-PANI ink which can be directly used for mask-assisted spray-coating. As a visualized demo, Figure S17 shows artistic patterns including school badge, high speed train, airplane, giant panda and flower obtained by spraying ss-PANI ink onto commercialized cellulose paper, indicating promising processability of 2D ss-PANI. Similarly, this ss-PANI can be easily processed into FSCs by spray coating method as vividly illustrated in Fig. 4b and Movie S2. Further, in combination with magnetic sputtering method, an Au thin film was incorporated as the current collector for developing the sandwiched FSCs.

As schematically shown in Fig. 4c, this as-developed FSC possesses the abundant interlayer space and quickly ion-transferring pathway, naturally demonstrating rapidly electrochemical responsibility. As expected, the average specific capacitance of the electrode can reach up to 377.5 F g^{-1} (Figure S18). The specific capacitance remains fundamentally unchanged versus various mass loading, indicating outstanding conductivity and it has the potential to package large-capacity supercapacitor. In Fig. 4d, 2D ss-PANI nanosheets maintain 65.8% of its initial specific capacitance with the scan rate increases from 5 to 100 mV s^{-1}. While in Fig. 4e, as the current density increases from 0.2 to 5 A g^{-1}, the capacitance retention rate reaches up to 66.7%. Such high rate-capability attributes to the reason that the unique 2D ss-PANI should facilitate rapid structure transitions of PANI from leucoemeraldine to polaronic emeraldine and further to pernigraniline [37]. CV and GCD of ss-PANI nanosheets are shown in Figure S19 a-b. The Nyquist comparison diagram of pure PANI and ss-PANI is shown in Figure S19c. The contact resistance of pure PANI is 5.86 Ω, while the ss-PANI is 3.68 Ω. In the low-frequency zone, slope of ss-PANI is much larger than that of pure PANI. Therefore, it can realize fast ion transfer, implying that the unique structure of ss-PANI could effectively promote the superior capacitive behavior and rate-capability [38,39]. Comparison of capacity retention of pure PANI and ss-PANI at different current densities can be seen in Figure S20. The capacity of ss-PANI can still maintain 76.9% after the current density of 0.5–5 A g^{-1} changes. In contrast, the capacity of pure PANI only maintains about 50.5%, which again confirms the high rate-capability of ss-PANI.

Besides, the areal capacitance of ss-PANI increases linearly with the increase of loading mass of the active substances (Figure S21). As the loading mass reaches to 1.03 mg cm^{-2}, the maximum areal capacitance of 337.5 mF cm^{-2} is obtained. In addition, this rate-capability is variable with the concentration of 1, 4-PDBA. Actually, ss-PANI prepared by the

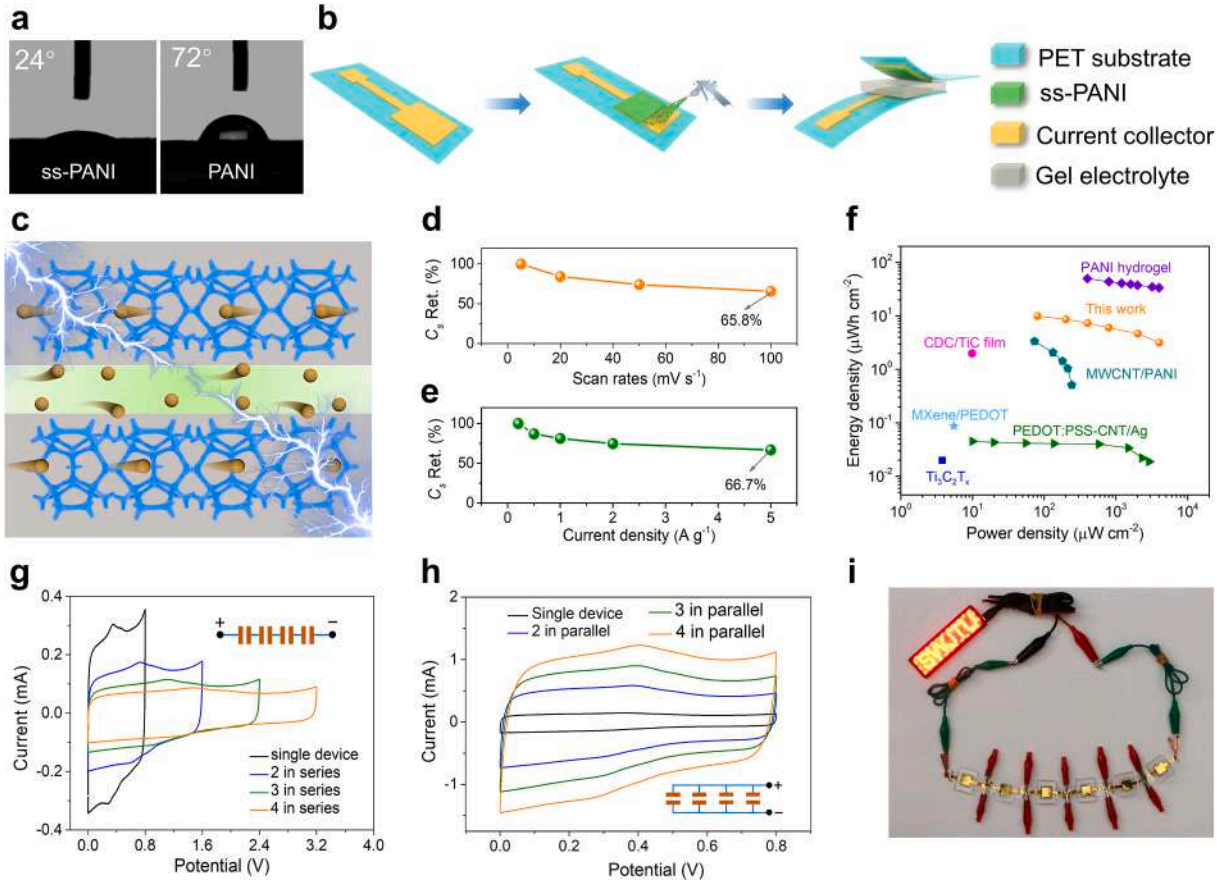

Fig. 4. Fabrication and electrochemical properties of ss-PANI based FSCs. (a) Comparison of water contact angles between pure PANI and 2D ss-PANI. (b) Schematic illustration of the fabrication process of individual FSC. (c) Numerous large inter-layer space of ss-PANI nanosheets facilitate ion transport and diffusion. Capacity retention varies with (d) different scan rates at 5, 20, 50, 100 mV s^{-1} and (e) current density at 0.2, 1, 2, 5 A g^{-1}. (f) Ragone plots of ss-PANI in comparison with other reported works. CV curves of one or more devices connected (g) in series and (h) in parallel at scan rate of 20 mV s^{-1}. (i) Photographs show the lamp brand powered by several devices connected in series.

1, 4-PDBA concentration of 0.005 mol L^{-1} exhibits the best electrochemical performance in comparison with others (Figure S22 a-f). The resulted high energy storage capability of ss-PANI is largely due to evenly distributed framework via the crosslink action of 1, 4-PDBA, which enables smooth entrance of the electrolyte ions to migration and hence makes full use of the active substances. Moreover, strong π-π conjugation between PANI and 1, 4-PDBA provides a much simpler ion-diffusion pathway, which promotes rapidly charge-transferring and leads to remarkably improved charging/discharging rate-capability [40–42]. However, due to the fact that 1, 4-PDBA is not an electrochemically active substance, higher concentration of 1, 4-PDBA will leads to the decrease of capacity. Therefore, a proper concentration (0.005 mol L^{-1}) of 1, 4-PDBA is demonstrated to obtain an optimized electrochemical performance.

In general, it is always a desired goal to obtain high power and energy densities simultaneously for FSCs. As shown in Fig. 4f, ss-PANI based FSCs clearly outperform other reported devices in terms of both power density and energy density [13,43–47]. This device shows a high energy density of 9.93 μWh cm^{-2} at a power density of 80 μW cm^{-2} and 3.16 μWh cm^{-2} at 4,000 μW cm^{-2} (Table S2). At the same time, it also demonstrates distinguished energy density of 1034.38 μWh cm^{-3} at power density of 8,333.33 μW cm^{-3} and 329.17 μWh cm^{-3} at power density of 416,666.67 μW cm^{-3} (Table S3), which displays wonderful rate capability under high current density. The series and parallel circuits evidently show the excellent integrability (Fig. 4g, h and S23a, b), stable performance and good homogeneity of as-prepared FSCs [48,49]. These integrated supercapacitors can also successfully light the LED bulb of 3.2 V (Figure S23c and Movie S3), LCD timer (Figure S23d), and a light board (Fig. 4i). Unambiguously, these above results will promote the promising practical application of ss-PANI FSCs.

However, as a typical pseudocapacitive material, conductive polymer PANI has structural disintegration, which limits its further application and development in flexible supercapacitors. Polyaniline is mostly zero-dimensional and one-dimensional material which have no secondary structures, most of them are prone to structural disintegration and failure due to volume expansion and contraction during charging/discharging (Fig. 5**a**). However, One-dimensional PANI with secondary structure could provide free volume, which could further withstand volume changes in the cycle process (Figure S24 and S25). Compared with one-dimensional materials, two-dimensional PANI nanosheets can provide larger inter-layer space and abundant free volume, which is conducive to ion adsorption and transport, and effectively buffers stress. The abundant free volume between adjacent secondary mastoid structure can effectively release the accumulated stress as the external stress is applied onto 2D ss-PANI nanosheets. As a result, the volume expansion/shrinkage arises from doping/de-doping mechanism can be remarkably eliminated due to the existence of the free volume in ss-PANI.

The volume expansion caused by the addition of ions and solvents is called as osmotic expansion [50]. The degree of expansion is strongly dependent on the type and the concentration of doping ions (and counter-ions). When the concentration of ions in the polymer changes, the osmotic pressure difference between the polymer and the electrolyte solution will be formed gradually. The increased osmotic pressure can push more water molecules into the polymer phase, resulting in an increase in polymer volume. In addition, the variable of bond length caused by ion doping and the intrinsic expansion of molecular conformation also contribute to volume change. The primarily internal osmotic stress must cause breaking, crushing or separated phenomena of the active material, thus significantly reducing the cyclic stability of electrode material. While in our strategy, 2D ss-PANI nanosheets share rich secondary structure, the volume expansion during charging/discharging processes can be alleviated effectively. There is abundant free volume between adjacent secondary mastoid structure (Fig. 5b). This free volume can effectively release the accumulated stress as the external stress is applied onto 2D ss-PANI nanosheets. As a result, the

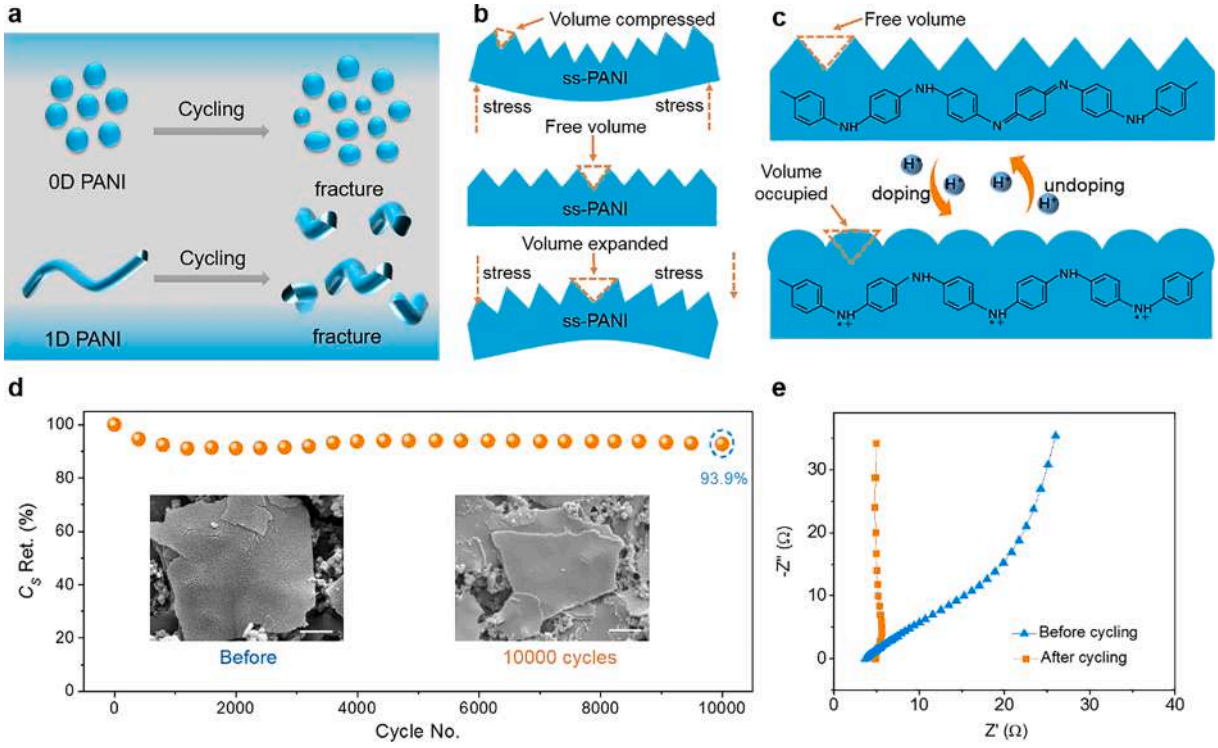

Fig. 5. Stability mechanism and cycling performance of ss-PANI based FSCs. (a) The structural disintegration of traditional conductive polymers leads to poor cyclic stability. (b) Free volume between adjacent secondary mastoid structure can stabilized the ss-PANI through mitigating stress accumulation. (c) During doping/dedoping processes, the secondary structure effectively mitigated the volume change. (d) Cycling stability of ss-PANI based FSC. The inset shows morphology unchanged before and after cycling. (e) EIS plots of ss-PANI based FSC before and after cycling.

volume expansion/shrinkage arises from doping/de-doping mechanism can be remarkably eliminated due to the existence of the free volume in ss-PANI (Fig. 5c).

Amazingly, the ss-PANI based FSC remains 93.9% of its initial capacitance after 10,000 cycles a current density of 1 mA cm^{-2}, and outperforms many other works (Table S4) [14,16,22,51,52], illuminating its excellent cycle stability (Fig. 5d). Even after 10,000 cycles, the morphology of ss-PANI has hardly changed, obviously revealing the excellent electrochemically structured stability of ss-PANI device (inset of Fig. 5d). Moreover, the self-reinforced PANI originated from rich secondary structure of supraparticles plays a significant role in restraining volume changes and accordingly improving cycling stability [53].

With impedance spectroscopy it is possible to get information of charge-transfer and diffusion processes. In the low-frequency zone, the tilt angle is nearly 90°, almost perpendicular to the X-axis (Fig. 5e), indicating that the device after cycling has good capacitance characteristics, which is mainly because the diffusion and migration of ions play a dominant role in the low-frequency region [54]. After the charging/discharging cycles, the ions in the electrolyte can be fully diffused and conducive to the rapid ion transmission and facilitate high cycling stability of ss-PANI FSCs [39]. Meanwhile, the internal resistance and charge transfer resistance after 10,000 cycles is significantly reduced compared with that before the cycle due to ion insertion.

In order to investigate the mechanical durability of ss-PANI based FSCs, we have investigated electrochemical performance of FSCs with multifarious mechanical loadings. After 100 cycles of consecutive bending, the capacitance retention maintained as high as 82.3% (Figure S26). Using diverse mechanical loadings such as bending and twisting, the devices show the unchanging CV curves as that of flatted device (Figure S27). Hence, ss-PANI based FSCs also possess the outstanding electrochemically mechanical stability [55,56].

3. Conclusions

In summary, a dynamically evolving emulsion supramolecular strategy was employed to successfully construct 2D ss-PANI. The unique structure restrains volume expansion and facilitates rapid ion diffusion. Its excellent volume durability and the intermolecular hydrogen bonding effect synergistically improved the anti-volume-changing ability during repeatedly charging/discharging process. The developed 2D ss-PANI-based FSCs presents a remarkable cycling stability of 93.9% capacitance retention over 10,000 galvanostatic charge/discharge cycles. Besides, this FSC exhibits high rate-capability along with a high specific capacitance of 378F g^{-1}. Undoubtedly, this work paves the way for fabricating novel structured PANI with superior electrochemical properties, which will give inspiration for promoting next-generation flexible power supplies.

4. Experimental

4.1. Materials

Aniline and 1,4-phenylenediboronic acid were purchased from Aladdin. N-N dimethyl acetamide, hydrochloric acid and ammonium persulfate (APS) were purchased from Chengdu Kelong chemical reagent factory. All the reagents were analytical grade and used as received without further purification.

4.2. Synthesis of ss-PANI

The ss-PANI materials were synthesized by a supramolecular crosslinking strategy based on an emulsion method. In a typical process, 0.286 g APS was dissolved in 1 mL distilled water, denoted as solution A. 0.0029 g of 1,4-phenylenediboronic acid was added into 1 mL deionized water, 2 mL N-N dimethyl acetamide and 500 μL of 6 M HCl, stirred until completely dissolved, labeled it solution B. N-N dimethyl acetamide can dissolve p-phenyldiboric acid, while hydrochloric acid is used to provide an acidic environment for proton doping. Sequentially, 321 μL aniline was slowly added into solution B and stirred for 3 min until it became clear. Both solution A and solution B were treated with ice bath for 30 min to let them cool down. Then, solution A was added into solution B to initiate aniline polymerization, stirred for 5 min until they were fully dispersed and kept the mixed solution in ice bath for 10–12 h for complete polymerization and crosslinking. Finally, the ss-PANI was purified by dialysis (dialysis tube, 14,000 MW cutoff) for 72 h to remove any by-products. 2D ss-PANI can be prepared under a wide range of 1,4-PDBA from 0.0005 to 0.3 mol L^{-1} (Figure S28) with colloid-forming process (Figure S29). 1, 4-PDBA with broad concentrations from 0.0005 to 0.3 mol L^{-1} yields unique 2D ss-PANI structure (Figure S30), which clearly verifies the crucial role of 1, 4-PDBA in self-assembling 2D morphology.

4.3. Characterizations

The morphology of the 2D ss-PANI was observed by scanning electron microscopy (JSM-7800f Prime) under the condition of vacuum of 9.6×10^{-5} Pa, acceleration voltage of 5 kV and working distance of 10 mm. The type and distribution of elements in the material were performed using energy dispersive spectrometer (EDS probe of Oxford Instrument) with accelerating voltage of 15 kV and vacuum degree of 9.6×10^{-5} Pa. The samples were analyzed by Fourier transformed infrared spectrum (FTIR, BRUKER) at a resolution of 2 cm^{-1}, with the scanning range from 4,000 to 400 cm^{-1}. The electrical conductivity of the powder was measured by the four-probe method after pressing to sheet. X-ray diffraction (XRD) was characterized on X-ray diffractometer (PANalytical X'Pert Powder, The Netherlands) with Cu Kα target. The microstructure and morphology were confirmed by a high-resolution transmission electron microscopy (TEM, JEM-2100F) with accelerating voltage of 200 kV at high vacuum mode. The surface topography and roughness of materials were performed using Atomic force micrographs (AFM, Multimode 8, Bruker, Germany). X-ray photoelectron spectroscopy (XPS, PHI Quantear SXM, ULVAC-PH, Japan) measurements was adopted to indicate element content and chemical valence state in samples with the ion source of Ar and the ray source was selected as water-cooled focusing to monochromatic Al Kα rays. TG-DSC (METTLER 1100LF) was used to measure the samples with high purity N_2 and Ar as protective gases and the heating rate was 10 $^{o}C\ min^{-1}$.

4.4. Preparation of working electrode and flexible supercapacitors

To prepare a working electrode for three-electrode tests, a 40 μm polyethylene terephthalate (PET) film was employed as the flexible substrate. Gold thin film was then evaporated onto PET film serving as current collector through magnetron sputtering with a sputtering power of 40 W for 20 min (TRP-450, SKY Technology Development Co., Ltd. China). To point it out, we have strictly controlled the areal of gold current collector into 1×1 cm^2 through proper design of the mask for magnetron sputtering and the thickness of sprayed gold on electrode is 380 nm (Figure S31). The surface SEM image demonstrating the uniformity and continuity of the gold layer supported by PET substrate (Figure S32). Sequentially, ss-PANI dispersed into deionized water was sprayed onto the current collector to form the film. Notably, the loading mass of ss-PANI on single electrode can be precisely controlled through adjusting the spray volume of ss-PANI ink.

For a typical fabrication of FSCs, two pieces of electrode with the same ss-PANI loading were assembled into sandwich configuration with PVA/H_2SO_4 gel electrolyte in between. The device was finally encapsulated with polydimethylsiloxane (PDMS) using drop cast method in a pre-designed mould.

4.5. Electrochemical measurements

Electrochemical characterization such as cyclic voltammetry (CV) and galvanostatic charge–discharge (GCD), Electrochemical impedance spectroscopy (EIS) were measured by CHI660E electrochemical workstation, and the cycling stability was carried out on a multi-channel electrochemical testing system (Arbin, USA). In a three-electrode configuration, saturated calomel electrode (SCE), platinum foils and ss-PANI electrode, 1 M H_2SO_4 aqueous solution were used as the reference, counter electrode, working electrode, and the electrolyte, respectively. Electrochemical tests of encapsulated device are carried out in two-electrode system, in which two symmetrical electrodes were respectively connected with the positive and negative of the electrochemical workstation.

Declaration of Competing Interest

The authors declare that they have no known competing financial interests or personal relationships that could have appeared to influence the work reported in this paper.

Acknowledgements

The authors would like to acknowledge the National Natural Science Foundation of China (No. 51977185 and No. 51972277) and Sichuan Science and Technology Program (No. 20ZDYF2833 and 20ZDYF2478) and the Rising Researchers of Southwest Jiaotong University (No. 2682021CG021). We are gratitude for the equipment support and XPS characterization provided by Analysis and Testing Center of Southwest Jiaotong University and Ceshigo Research Service (https://www.ceshigo.com/), respectively.

Appendix A. Supplementary data

See supporting information for TG-DSC, XRD, SEM, TEM, electrochemical characterization, spraying display of ss-PANI, the process gelation of ss-PANI at different concentrations. Supplementary data to this article can be found online at https://doi.org/10.1016/j.cej.2021.130203.

References

[1] R. Haight, W. Haensch, D. Friedman, Solar-powering the internet of things, Science 353 (6295) (2016) 124–125.
[2] D.P. Dubal, N.R. Chodankar, D.-H. Kim, P. Gomez-Romero, Towards flexible solid-state supercapacitors for smart and wearable electronics, Chem. Soc. Rev. 47 (6) (2018) 2065–2129.
[3] G. Chen, Y. Li, M. Bick, J. Chen, Smart textiles for electricity generation, Chem. Rev. 120 (8) (2020) 3668–3720.
[4] R. Jia, G. Shen, F. Qu, D. Chen, Flexible on-chip micro-supercapacitors: efficient power units for wearable electronics, Energy Storage Mater. 27 (2020) 169–186.
[5] Q. Wang, F.Y. Liu, Z.Y. Jin, X.R. Qiao, H.C. Huang, X. Chu, D. Xiong, H.T. Zhang, Y. Liu, W.Q. Yang, Hierarchically divacancy defect building dual-activated porous carbon fibers for high-performance energy-storage devices, Adv. Funct. Mater. 30 (2020) 2002580.
[6] X. Lu, M. Yu, G. Wang, Y. Tong, Y. Li, Flexible solid-state supercapacitors: design, fabrication and applications, Energy Environ. Sci. 7 (2014) 2160–2181.
[7] K. Wang, X. Zhang, C. Li, H. Zhang, X. Sun, N. Xu, Y. Ma, Flexible solid-state supercapacitors based on a conducting polymer hydrogel with enhanced electrochemical performance, J. Mater. Chem. A 2 (2014) 19726–19732.
[8] C. Li, X. Zhang, Z. Lv, K. Wang, X. Sun, X. Chen, Y. Ma, Scalable combustion synthesis of graphene-welded activated carbon for high-performance supercapacitors, Chem. Eng. J. 414 (2021) 128781.
[9] C. Sun, X. Zhang, C. Li, K. Wang, X. Sun, Y. Ma, High-efficiency sacrificial prelithiation of lithium-ion capacitors with superior energy-storage performance, Energy Storage Mater. 24 (2020) 160–166.
[10] Y. Xu, K. Wang, J. Han, C. Liu, Y. An, Q. Meng, C. Li, X. Zhang, X. Sun, Y. Zhang, L. Mao, Z. Wei, Y. Ma, Scalable production of wearable solid-state li-ion capacitors from N-doped hierarchical carbon, Adv. Mater. 32 (2020) 2005531.
[11] Z. Xu, X. Chu, Y. Wang, H. Zhang, W. Yang, Three-dimensional polymer networks for solid-state electrochemical energy storage, Chem. Eng. J. 391 (2020), 123548.
[12] Y. Yang, A mini-review: emerging all-solid-state energy storage electrode materials for flexible devices, Nanoscale 12 (2020) 3560–3573.
[13] X. Chu, H. Huang, H. Zhang, H. Zhang, B. Gu, H. Su, F. Liu, Y.u. Han, Z. Wang, N. Chen, C. Yan, W. Deng, W. Deng, W. Yang, Electrochemically building three-dimensional supramolecular polymer hydrogel for flexible solid-state micro-supercapacitors, Electrochim. Acta 301 (2019) 136–144.
[14] Q. Wu, Y. Xu, Z. Yao, A. Liu, G. Shi, Supercapacitors based on flexible graphene/polyaniline nanofiber composite films, ACS Nano 4 (4) (2010) 1963–1970.
[15] H. Li, J. Wang, Q. Chu, Z. Wang, F. Zhang, S. Wang, Theoretical and experimental specific capacitance of polyaniline in sulfuric acid, J. Power Sources 190 (2009) 578–586.
[16] B. Yao, L. Yuan, X.u. Xiao, J. Zhang, Y. Qi, J. Zhou, J. Zhou, B. Hu, W. Chen, Paper-based solid-state supercapacitors with pencil-drawing graphite/polyaniline networks hybrid electrodes, Nano Energy 2 (6) (2013) 1071–1078.
[17] X. Zheng, L. Yao, Y. Qiu, S. Wang, K. Zhang, Core-sheath porous polyaniline nanorods/graphene fiber-shaped supercapacitors with high specific capacitance and rate capability, ACS Appl. Energy Mater. 2 (6) (2019) 4335–4344.
[18] X. Chu, X. Zhao, Y. Zhou, Y. Wang, X. Han, Y. Zhou, J. Ma, Z. Wang, H. Huang, Z. Xu, C. Yan, H. Zhang, W. Yang, J. Chen, An ultrathin robust polymer membrane for wearable solid-state electrochemical energy storage, Nano Energy 76 (2020), 105179.
[19] Y. Xie, X. Sha, Electrochemical cycling stability of nickel (II) coordinated polyaniline, Synthetic Met. 237 (2018) 29–39.
[20] C. Xia, W. Chen, X. Wang, M.N. Hedhili, N. Wei, H.N. Alshareef, Highly stable supercapacitors with conducting polymer core-shell electrodes for energy storage applications, Adv. Energy Mater. 5 (2015) 1401805.
[21] H. Zhang, J. Wang, Y. Chen, Z. Wang, S. Wang, Long-term cycling stability of polyaniline on graphite electrodes used for supercapacitors, Electrochim. Acta 105 (2013) 69–74.
[22] F. Jiang, W. Li, R. Zou, Q. Liu, K. Xu, L. An, J. Hu, MoO_3/PANI coaxial heterostructure nanobelts by in situ polymerization for high performance supercapacitors, Nano Energy 7 (2014) 72–79.
[23] P. Yu, Z. Zhang, L. Zheng, F. Teng, L. Hu, X. Fang, A novel sustainable flour derived hierarchical nitrogen-doped porous carbon/polyaniline electrode for advanced asymmetric supercapacitors, Adv. Energy Mater. 6 (2016) 1601111.
[24] X. Meng, D. Qiu, Fabrication of monodisperse asymmetric polystyrene particles by crosslinking regulation in seeded emulsion polymerization, Polymer 203 (2020), 122799.
[25] T. Watanabe, Y. Nishizawa, H. Minato, C. Song, K. Murata, D. Suzuki, Hydrophobic monomers recognize microenvironments in hydrogel microspheres during free-radical-seeded emulsion polymerization, Angew. Chem. Int. Edit. 59 (23) (2020) 8849–8853.
[26] W. Lu, X. Le, J. Zhang, Y. Huang, T. Chen, Supramolecular shape memory hydrogels: a new bridge between stimuli-responsive polymers and supramolecular chemistry, Chem. Soc. Rev. 46 (2017) 1284–1294.
[27] Z. Zhang, Z. Wei, M. Wan, Nanostructures of polyaniline doped with inorganic acids, Macromolecules 35 (15) (2002) 5937–5942.
[28] L. Zhang, M. Wan, Self-assembly of polyaniline-from nanotubes to hollow microspheres, Adv. Funct. Mater. 13 (10) (2003) 815–820.
[29] Z. Wei, L. Zhang, M. Yu, Y. Yang, M. Wan, Self-assembling sub-micrometer-sized tube junctions and dendrites of conducting polymers, Adv. Mater. 15 (16) (2003) 1382–1385.
[30] L. Zhang, L. Zhang, M. Wan, Y. Wei, Polyaniline micro/nanofibers doped with saturation fatty acids, Synthetic Met. 156 (5-6) (2006) 454–458.
[31] W. Wu, D. Pan, Y. Li, G. Zhao, L. Jing, S. Chen, Facile fabrication of polyaniline nanotubes using the self-assembly behavior based on the hydrogen bonding: a mechanistic study and application in high-performance electrochemical supercapacitor electrode, Electrochim. Acta 152 (2015) 126–134.
[32] G.H. Lim, H.J. Choi, Synthesis of self-assembled rectangular-shaped polyaniline nanotubes and their physical characteristics, J. Ind. Eng. Chem. 47 (2017) 51–55.
[33] K.G.C. Senarathna, M.M.M.G.P.G. Mantilaka, T.A.N. Peiris, H.M.T.G.A. Pitawala, D.G.G.P. Karunaratne, R.M.G. Rajapakse, Convenient routes to synthesize uncommon vaterite nanoparticles and the nanocomposites of alkyd resin/polyanifine/vaterite: The latter possessing superior anticorrosive performance on mild steel surfaces, Electrochim. Acta 117 (2014) 460-469.
[34] R.M.N.M. Rathnayake, M.M.M.G.P.G. Mantilaka, M. Hara, H.H. Huang, H.W.M.A. C. Wijayasinghe, M. Yoshimura, H.M.T.G.A. Pitawala, Graphite intercalated polyaniline composite with superior anticorrosive and hydrophobic properties, as protective coating material on steel surfaces, Appl. Surf. Sci. 410 (2017) 445-453.
[35] J. Yan, T. Wei, B.o. Shao, Z. Fan, W. Qian, M. Zhang, F. Wei, Preparation of a graphene nanosheet/polyaniline composite with high specific capacitance, Carbon 48 (2) (2010) 487–493.
[36] Y. Tian, Y. Wang, Y. Wang, L. Ma, X. Gao, Utilizing polyaniline to decorate graphene and its effect on the electrochemical properties of polyaniline/graphene electrode composite, Mater. Res. Express 6 (2019), 105614.
[37] G. Ćirić-Marjanović, Recent advances in polyaniline research: polymerization mechanisms, structural aspects, properties and applications, Synthetic Met. 177 (2013) 1–47.
[38] J. Xu, K. Wang, S.Z. Zu, B.H. Han, Z. Wei, Hierarchical nanocomposites of polyaniline nanowire arrays on graphene oxide sheets with synergistic effect for energy storage, ACS Nano 4 (9) (2010) 5019–5026.
[39] Q. Zhou, X.M. Su, H. Zhang, Y.J. Weng, Characterization of electrochemically synthesized pani on graphite electrode use EIS, Adv. Mater. Res. 295-297 (2011) 1124–1128.
[40] O. Sadak, M.U.A. Prathap, S. Gunasekaran, Facile fabrication of highly ordered polyaniline–exfoliated graphite composite for enhanced charge storage, Carbon 144 (2019) 756–763.

[41] H.P. Cong, X.C. Ren, P. Wang, S.H. Yu, Flexible graphene–polyaniline composite paper for high-performance supercapacitor, Energy Environ. Sci. 6 (4) (2013) 1185–1191.
[42] Z. Tong, Y. Yang, J. Wang, J. Zhao, B.-L. Su, Y. Li, Layered polyaniline/graphene film from sandwich-structured polyaniline/graphene/polyaniline nanosheets for high-performance pseudosupercapacitors, J. Mater. Chem. A 2 (13) (2014) 4642–4651.
[43] P. Huang, C. Lethien, S. Pinaud, K. Brousse, R. Laloo, V. Turq, M. Respaud, A. Demortiere, B. Daffos, P.L. Taberna, B. Chaudret, Y. Gogotsi, P. Simon, On-chip and freestanding elastic carbon films for micro-supercapacitors, Science 351 (6274) (2016) 691–695.
[44] L. Li, Z. Lou, W. Han, D. Chen, K. Jiang, G. Shen, Highly stretchable micro-supercapacitor arrays with hybrid MWCNT/PANI electrodes, Adv. Mater. Technol. 2 (2017) 1600282.
[45] J. Li, A. Levitt, N. Kurra, K. Juan, N. Noriega, X.u. Xiao, X. Wang, H. Wang, H. N. Alshareef, Y. Gogotsi, MXene-conducting polymer electrochromic microsupercapacitors, Energy Storage Mater. 20 (2019) 455–461.
[46] W. Liu, C. Lu, H. Li, R.Y. Tay, L. Sun, X. Wang, W.L. Chow, X. Wang, B.K. Tay, Z. Chen, J.i. Yan, K. Feng, G. Lui, R. Tjandra, L. Rasenthiram, G. Chiu, A. Yu, Paper-based all-solid-state flexible micro-supercapacitors with ultra-high rate and rapid frequency response capabilities, J. Mater. Chem. A 4 (10) (2016) 3754–3764.
[47] H. Huang, J. He, Z. Wang, H. Zhang, L. Jin, N. Chen, Y. Xie, X. Chu, B. Gu, W. Deng, W. Yang, Scalable, and low-cost treating-cutting-coating manufacture platform for MXene-based on-chip micro-supercapacitors, Nano Energy 69 (2020), 104431.
[48] M.M. Pérez-Madrigal, F. Estrany, E. Armelin, D.D. Díaz, C. Alemán, Towards sustainable solid-state supercapacitors: electroactive conducting polymers combined with biohydrogels, J. Mater. Chem. A 4 (2016) 1792–1805.
[49] H. Hu, Z. Pei, H. Fan, C. Ye, 3D interdigital Au/MnO_2/Au stacked hybrid electrodes for on-chip microsupercapacitors, Small 12 (22) (2016) 3059–3069.
[50] T. Liu, Y. Li, Addressing the achilles' heel of pseudocapacitive materials: long-term stability, InfoMat 2 (2020) 807–842.
[51] H. Hu, K. Zhang, S. Li, S. Ji, C. Ye, Flexible, in-plane, and all-solid-state micro-supercapacitors based on printed interdigital Au/polyaniline network hybrid electrodes on a chip, J. Mater. Chem. A 2 (48) (2014) 20916–20922.
[52] T. Dai, Y. Jia, Supramolecular hydrogels of polyaniline-poly(styrene sulfonate) prepared in concentrated solutions, Polymer 52 (12) (2011) 2550–2558.
[53] S. Grover, S. Goel, V. Sahu, G. Singh, R.K. Sharma, Asymmetric supercapacitive characteristics of PANI embedded holey graphene nanoribbons, ACS Sustain. Chem. Eng. 3 (7) (2015) 1460–1469.
[54] S.M. Park, J.S. Yoo, Electrochemical impedance spectroscopy for better electrochemical measurements, Anal. Chem. 75 (2003) 455a–461a.
[55] G.P. Hao, F. Hippauf, M. Oschatz, F.M. Wisser, A. Leifert, W. Nickel, N. Mohamed-Noriega, Z. Zheng, S. Kaskel, Stretchable and Semitransparent Conductive Hybrid Hydrogels for Flexible Supercapacitors, ACS Nano 8 (2014) 7138–7146.
[56] Q. Wang, Y.H. Zhou, X. Zhao, K. Chen, B.N. Gu, T. Yang, H.T. Zhang, W.Q. Yang, J. Chen, Tailoring Carbon Nanomaterials via a Molecular Scissor, Nano Today 36 (2021) 101033.